Mathematics

https://www.aimspress.com/journal/Math

AIMS Mathematics, 10(11): 26389–26417.
DOI: 10.3934/math.20251160
Received: 18 August 2025
Revised: 22 October 2025
Accepted: 06 November 2025
Published: 14 November 2025

Research article

A mixed local discontinuous Galerkin scheme for capturing shock-driven instabilities in compressible multicomponent flows

Salman Saud Alsaeed[1] **and Satyvir Singh**[2,3,*]

[1] Department of Mathematics, Jouf University, Sakaka P.O. Box 2014, Saudi Arabia
[2] Institute for Applied and Computational Mathematics, RWTH Aachen University, Germany
[3] Department of Mathematics, Graphic Era Deemed to be University, Dehradun, Uttarakhand, India

* **Correspondence:** Email: singh@acom.rwth-aachen.de.

Abstract: This study proposes a mixed local discontinuous Galerkin (LDG) scheme for capturing shock-driven interfacial instabilities in compressible multicomponent flows. The proposed scheme is validated through canonical test cases, including sod shock tube, shock-driven light/heavy cylinders, and chevron-shaped, and shows excellent agreement with experimental and numerical benchmarks. It effectively captures key mechanisms including shock refraction, baroclinic vorticity generation, vortex roll-up, and nonlinear interface evolution. A systematic parametric analysis is carried out for the single-mode heavy fluid layer configuration to examine the impact of interface thickness on shock-driven instability development. The results reveal that thinner interfaces intensify baroclinic vorticity deposition and accelerate the transition to nonlinear stages, whereas thicker interfaces delay instability growth and mitigate small-scale structure formation. Spatially-integrated measures of baroclinic vorticity and enstrophy further confirm that geometric confinement plays a pivotal role in regulating vortex evolution and interfacial mixing.

Keywords: shock-driven instability; multicomponent compressible flows; mixed local discontinuous Galerkin; shock wave; baroclinic vorticity
Mathematics Subject Classification: 76L05, 76M22, 76T10

---

1. Introduction

Compressible multicomponent flows are characterized by the simultaneous presence of distinct species or phases whose density, composition, and thermodynamic properties may vary sharply in space and time. In high-speed applications, such as shock-interface interactions, the propagation of compression waves through heterogeneous mixtures induces complex interfacial dynamics driven by baroclinic vorticity production, species diffusion, and differences in acoustic impedance [1–3].

Unlike single-component flows, multicomponent systems require accounting for additional transport mechanisms that govern mass fraction evolution, which in turn alters local density gradients and modifies the strength and morphology of the instability [4,5]. The accurate prediction of these coupled processes therefore relies on solving the full compressible viscous multicomponent equations, which enable the inclusion of stresses, heat conduction, and diffusive fluxes [6]. This integrated framework offers a physically coherent representation of shock-interface interactions and serves as a vital tool for analyzing the initiation and development of hydrodynamic instabilities in both engineering and physical contexts [7–10].

Shock-driven instability occurs when a shock wave strikes a perturbed density interface, creating misaligned gradients of pressure and density that generate baroclinic vorticity and initiate a complex post-shock flow evolution. This phenomenon is widely referred to as the Richtmyer-Meshkov (RM) instability [11, 12], which represents the impulsive counterpart of the buoyancy-driven Rayleigh-Taylor (RT) instability. After the initial shock impact, the post-shock shear layers trigger the development of Kelvin-Helmholtz (KH) instability, further amplifying perturbations and promoting roll-up of vortical structures, which accelerates mixing and transition to turbulence. In multicomponent configurations, the mechanical impulse imparted by the incident shock amplifies initial perturbations at the interface, leading to rapid deformation and complex vortex dynamics. The growth of these instabilities depends strongly on the incident Mach number, initial perturbation wavelength, Atwood number, and transport effects, making it highly sensitive to the physical properties of the participating species [13, 14]. Moreover, secondary reshock events can significantly enhance mixing by generating additional vorticity and energizing smaller scales of motion [15]. Accurate numerical prediction of shock-driven instabilities therefore requires high-fidelity methods capable of resolving sharp gradients and capturing interfacial topology changes without excessive numerical dissipation.

Shock-driven interfaces in compressible multicomponent flows exhibit complex dynamics due to the interplay of sharp material discontinuities, baroclinic vorticity generation, and multiscale interfacial deformation [16]. Accurately resolving these mechanisms within a numerical framework requires high-order spatial discretization schemes with very low dissipation and dispersion errors. However, conventional shock-capturing methods tend to smear interface morphology and damp the evolution of small-scale vortical structures, leading to an underprediction of the instability growth rate and mixing intensity [17]. The impulsive deposition of baroclinic vorticity induces both the RM and subsequent KH type instabilities, which rapidly generate high-wave-number features that demand fine spatial resolution and robust limiter strategies to avoid spurious oscillations [18, 19]. These requirements pose serious challenges in the development of numerical schemes that simultaneously ensure stability at discontinuities and preserve spectral-like resolution in smooth regions [20, 21].

In multicomponent configurations, additional complications are introduced by variable thermodynamic properties, stiff diffusive transport, and the strong coupling between species concentration and density gradients [22]. Even small levels of numerical dissipation may artificially suppress the formation of secondary instability structures behind the shock and alter the interfacial roll-up behavior. Furthermore, repeated shock-interface interactions (reshocks) significantly amplify high-frequency perturbations, making the simulation highly sensitive to mesh resolution and flux reconstruction accuracy [23]. These challenges underscore the necessity of high-order schemes equipped with carefully designed limiters or artificial viscosity procedures to guarantee stability while preserving the physically relevant small-scale features of shock-induced instability.

The main objective of this study is to establish a high-fidelity numerical framework that can precisely resolve the nonlinear progression of shock-induced instabilities in compressible multicomponent flows. Although a wide variety of shock-interface configurations have been examined using classical finite-volume and finite-difference approaches [24–26], many of these methods suffer from excessive numerical diffusion, which can artificially smear small-scale vortical structures and result in inaccurate predictions of baroclinic vorticity generation and interfacial mixing. In particular, the accurate resolution of coupled RM and KH mechanisms requires numerical schemes that offer both high spectral accuracy and inherent shock-capturing capability. To overcome these limitations, the present study proposes a high-order mixed modal discontinuous Galerkin scheme that combines excellent spectral accuracy in smooth regions with robust limiters at sharp density interfaces. The scope of this work includes the formulation of the multicomponent local discontinuous Galerkin (LDG) discretization, its validation against canonical benchmark problems, and its application to the simulation of the RM instability, with detailed analysis of interface morphology, baroclinic vorticity dynamics, and the influence of transport properties.

The structure of the paper is as follows. Section 2 presents the governing equations for compressible multicomponent Navier-Stokes-Fourier (NSF) flows along with the corresponding thermodynamic relationships. Section 3 describes the mixed modal discontinuous Galerkin formulation in detail, including spatial discretization, numerical fluxes, limiter strategy, and time-integration procedure. To illustrate the precision and resilience of the suggested approach, a series of validation studies on standard shock-interface combinations are shown in Section 4. The evolution of interface morphology, the creation of baroclinic vorticities, and the impact of interface thickness and perturbation amplitude are examined in the applications to a canonical RM instability that are also reported. Section 5 concludes by summarizing the key conclusions and suggesting potential avenues for further study.

2. Governing equations

In the present study, we focus on an ideal, non-reactive multicomponent gas mixture and model its temporal evolution using the two-dimensional unsteady compressible NSF equations [6, 27]. This mathematical framework accounts for the conservation of mass, momentum, and energy in conjunction with appropriate constitutive relations for viscosity, thermal conductivity, and species diffusion. By employing this formulation, the coupled effects of compressibility, viscous dissipation, and heat transfer can be accurately captured, providing a physically consistent description of the shock-interface interaction in multicomponent environments. Let

$$\mathbf{U} = [\rho, \rho\mathbf{u}, \rho E, \rho Y_k]^T \tag{2.1}$$

denote the vector of conserved variables, where ρ is the density, $\mathbf{u}$ the velocity field, E the total specific energy, and Y_k the mass fraction of the kth species.

The governing equations can then be compactly expressed as a system of conservation laws,

$$\frac{\partial \mathbf{U}}{\partial t} + \nabla \cdot \mathbf{F}_{\mathrm{c}}(\mathbf{U}) + \nabla \cdot \mathbf{F}_{\mathrm{d}}(\mathbf{U}, \Pi, \mathbf{Q}) = 0, \tag{2.2}$$

where $\mathbf{F}_{\mathrm{c}}$ and $\mathbf{F}_{\mathrm{d}}$ stand for the convective and diffusive flux components, respectively. These flux components are given by

$$\mathbf{F}_{\mathrm{c}} = [\rho\mathbf{u}, \rho\mathbf{u}\mathbf{u} + p\mathbf{I}, (\rho E + p)\mathbf{u}, \rho Y_k\mathbf{u}]^T, \tag{2.3}$$

$$\mathbf{F}_{\mathrm{d}} = \left[0, \Pi, \Pi \cdot \mathbf{u} + \mathbf{Q}, \rho D_k \nabla Y_k\right]^T . \tag{2.4}$$

Here, p denotes the thermodynamic pressure, $\mathbf{I}$ is the identity tensor, and D_k is the diffusion coefficient of the kth species. The viscous stress tensor Π and the heat flux vector $\mathbf{Q}$ are modeled by a Newtonian constitutive law and Fourier's law, respectively. To this end, we introduce the deviatoric strain-rate tensor

$$\mathbf{S} = \frac{1}{2}\left(\nabla\mathbf{u} + (\nabla\mathbf{u})^T\right) - \frac{1}{3}(\nabla\cdot\mathbf{u})\,\mathbf{I}, \tag{2.5}$$

and express the stress and heat flux as

$$\Pi = -\,2\mu\,\mathbf{S}, \qquad \mathbf{Q} = -\,\kappa\,\nabla T, \tag{2.6}$$

where μ and κ represent the dynamic viscosity and thermal conductivity of the gas mixture, respectively, and T denotes the temperature. The mixture composition is described via the mass fraction, defined as $Y_k = \rho_k/\rho$. For a two-species system, one may simply set $Y_1 = 1 - Y_2$. The total energy density is written as

$$\rho E = \frac{p}{\bar{\gamma} - 1} + \frac{1}{2}\rho|\mathbf{u}|^2, \tag{2.7}$$

where $\bar{\gamma}$ denotes the effective ratio of specific heats of the mixture. This quantity is obtained from the mixture-averaged specific heat capacities at constant pressure and constant volume, namely

$$\bar{C}_p = \sum_k z_k\, C_{p,k}, \qquad \bar{C}_v = \sum_k z_k\, C_{v,k}, \qquad \bar{\gamma} = \frac{\bar{C}_p}{\bar{C}_v}, \tag{2.8}$$

with $z_k = Y_k/M_k$ representing the normalized mass fraction of species k. The individual species' heat capacities follow the ideal-gas relations

$$C_{p,k} = \frac{\gamma_k R_u}{\gamma_k - 1}, \qquad C_{v,k} = C_{p,k} - R_u, \tag{2.9}$$

where R_u denotes the universal gas constant. The mixture pressure is obtained using Dalton's law, such that $p = \sum_k p_k$ with $p_k = \rho_k R_k T$. The transport properties of the mixture are computed through mass-weighted averaging, i.e.,

$$(\bar{\mu},\ \bar{\kappa}) = \left(\frac{\sum_k \mu_k Y_k M_k^{-1/2}}{\sum_k Y_k M_k^{-1/2}},\ \frac{\sum_k \kappa_k Y_k M_k^{-1/2}}{\sum_k Y_k M_k^{-1/2}}\right). \tag{2.10}$$

The viscosity of each species is determined using a Chapman-Enskog formulation [28],

$$\mu_k = C_\mu\,\frac{\sqrt{M_k T}}{\Omega_{\mu,k}\,\sigma_k^2}, \qquad C_\mu = 2.6693\times 10^{-6}, \tag{2.11}$$

where σ_k denotes the molecular collision diameter and $\Omega_{\mu,k}$ represents the temperature-dependent collision integral. The thermal conductivity of each species is obtained via its corresponding Prandtl number,

$$\kappa_k = \frac{C_{p,k}}{Pr_k}\,\mu_k. \tag{2.12}$$

The binary diffusion coefficient for species i and j is evaluated as

$$D_{ij} = \frac{0.0266}{\Omega_D} \frac{T^{3/2}}{p\,\sqrt{M_{ij}}\,\sigma_{ij}^2}, \tag{2.13}$$

where $M_{ij} = \frac{2M_iM_j}{M_i+M_j}$ and $\sigma_{ij} = \frac{1}{2}(\sigma_i + \sigma_j)$.

The species viscosity is evaluated by means of a Chapman-Enskog type expression [29],

$$\mu_k = C_\mu \frac{\sqrt{M_kT}}{\sigma_k^2} \Phi_\mu^{-1}(T_k^\star), \qquad C_\mu = 2.6693 \times 10^{-6}, \tag{2.14}$$

where $T_k^\star = T/(\epsilon/K_B)_k$ is the normalized temperature and $\Phi_\mu(\cdot)$ denotes the temperature-dependent collision-integral function

$$\Phi_\mu(T^\star) = A_\mu(T^\star)^{-B_\mu} + C_\mu^\star \exp\Big(-D_\mu T^\star\Big) + E_\mu \exp\Big(-F_\mu T^\star\Big), \tag{2.15}$$

with $(A_\mu, B_\mu, C_\mu^\star, D_\mu, E_\mu, F_\mu) = (1.161, 0.149, 0.525, 0.773, 2.162, 2.438)$. Thermal conductivity for species k is related to the viscosity via

$$\kappa_k = \frac{C_{p,k}}{Pr_k}\mu_k. \tag{2.16}$$

The mass-diffusion coefficient of a binary mixture is written as

$$D_{ij} = C_D \frac{T^{3/2}}{p\,\sqrt{M_{ij}}\,\sigma_{ij}^2} \Phi_D^{-1}(T_{ij}^\star), \qquad C_D = 0.0266, \tag{2.17}$$

where $M_{ij} = 2M_iM_j/(M_i + M_j)$, $\sigma_{ij} = \frac{1}{2}(\sigma_i + \sigma_j)$, and $T_{ij}^\star = \sqrt{(\epsilon_i/K_B)(\epsilon_j/K_B)}$. The function Φ_D represents the diffusion collision integral and is approximated by [6]

$$\Phi_D(T^\star) = A_D(T^\star)^{-B_D} + C_D^\star \exp(-D_DT^\star) + E_D \exp(-F_DT^\star) + G_D \exp(-H_DT^\star), \tag{2.18}$$

with the parameter values

$$(A_D, B_D, C_D^\star, D_D, E_D, F_D, G_D, H_D) = (1.060, 0.156, 0.193, 0.476, 1.036, 1.530, 1.765, 3.894). \tag{2.19}$$

3. Numerical methodology

The accuracy and robustness of shock-resolved NSF simulations in multicomponent flows strongly depend on the choice of spatial discretization and the treatment of diffusive terms. This work adopts a mixed LDG approach for the first-order reformulation of the compressible NSF equations, consistent with the LDG framework introduced by Cockburn and Shu [30]. The use of alternating numerical fluxes for diffusive terms and auxiliary gradient variables follows the standard LDG strategy, ensuring local conservation and stability while maintaining compatibility with high-order polynomial representations.

3.1. Mixed formulation

Because the viscous contribution introduces second-order spatial derivatives, the governing equation Eq (2.2) is recast into an equivalent first-order form by introducing an auxiliary variable **G**, as commonly employed in mixed LDG approaches [31, 32]. This auxiliary field represents the local gradient of the solution variables and is added to the system in order to treat the diffusive terms consistently within the LDG framework. The resulting first-order system reads

$$\begin{aligned} &\mathbf{G} - \nabla \mathbf{U} = 0, \\ &\frac{\partial \mathbf{U}}{\partial t} + \nabla \cdot \mathbf{F}_{\mathrm{c}}(\mathbf{U}) + \nabla \cdot \mathbf{F}_{\mathrm{d}}(\mathbf{U}, \mathbf{G}) = 0, \end{aligned} \tag{3.1}$$

which expresses both the convective and diffusive fluxes in terms of first-order derivatives and is therefore well suited for a modal elementwise discretization.

3.2. Numerical approximation and function space

We discretize the computational domain $\Omega \subset \mathbb{R}^2$ using a mesh Ω_h composed of non-overlapping rectangular elements such that Ω_h forms a partition of Ω. The set of inter-element boundaries is denoted by $\mathcal{E}_h$. To define the discrete function space, we introduce the reference element $\hat{I}^2 = [-1, 1] \times [-1, 1]$ with local coordinates $\boldsymbol{\xi} = (\xi, \eta)$ and the reference edge $\hat{I} = [-1, 1]$. The mappings $\mathbf{x}_m(\boldsymbol{\xi})$ associate the reference element and its edge with their corresponding physical element and edge in the mesh Ω_h. The approximate solutions for Eq (3.1) are constructed in a space of piecewise polynomial functions, defined as

$$\mathcal{V}_h^p = \left\{ \phi \in L^2(\Omega_h) \;:\; \phi|_{\Omega_m} \circ \mathbf{x}_m(\boldsymbol{\xi}) \in Q^p(\hat{I}^2), \;\; \forall\, \Omega_m \in \Omega_h \right\}, \tag{3.2}$$

where $Q^p(\hat{I}^2)$ denotes the tensor-product polynomial space over the reference element $\hat{I}^2$, consisting of all polynomials of degree at most p in each coordinate direction.

$$\begin{aligned} \mathbf{U}_h(\mathbf{x}, t) &:= \sum_{i,j=0}^{p} \phi_m^{ij}(\mathbf{x})\, \mathbf{U}_m^{ij}(t), \\ \mathbf{G}_h(\mathbf{x}, t) &:= \sum_{i,j=0}^{p} \phi_m^{ij}(\mathbf{x})\, \mathbf{G}_m^{ij}(t), \qquad \forall\, \mathbf{x} \in m, \;\; m \in \Omega_h, \;\; t \geq 0, \end{aligned} \tag{3.3}$$

where $\{\phi_n^{ij}\}_{0 \leq i,j \leq p}$ forms a basis of $\mathcal{V}_h^p$ on element m and has dimension $(p+1)^2$. The coefficients $\{\mathbf{U}_m^{ij}\}_{0 \leq i,j \leq p}$ and $\{\mathbf{G}_m^{ij}\}_{0 \leq i,j \leq p}$ represent the corresponding modal degrees of freedom. Let $\{\psi_i(\xi)\}_{i=0}^{p}$ denote the orthonormal scaled Legendre polynomials defined on the reference interval $I = [-1, 1]$, i.e., $-1 = \xi_0 < \xi_1 < \cdots < \xi_p = 1$. The two-dimensional basis functions are constructed as tensor products of the one-dimensional modal Legendre polynomials

$$\phi_{ij}(\mathbf{x}) = \psi_i(\xi)\, \psi_j(\eta), \qquad 0 \leq i, j \leq p, \tag{3.4}$$

where

$$\psi_i(\xi) = \frac{2(i!)^2}{(2i)!}\, P_i(\xi), \qquad \psi_j(\eta) = \frac{2(j!)^2}{(2j)!}\, P_j(\eta),$$

with $P_i(\xi)$ and $P_j(\eta)$ denoting the classical Legendre polynomials. It is emphasized that the present formulation employs a purely modal representation, where the solution coefficients are evolved in the modal space without nodal interpolation during flux evaluation or time integration. For post-processing and visualization, the numerical solutions are sampled at the cell centers to provide a clear and uniform representation of the flow variables.

Although a total-degree basis $\mathbb{P}^p$ contains fewer degrees of freedom ($(p+1)(p+2)/2$) compared to the tensor-product basis $\mathbb{Q}^p$ ($(p+1)^2$), the present formulation employs $\mathbb{Q}^p$ polynomials owing to several practical advantages. First, the $\mathbb{Q}^p$ basis leads to a diagonal mass matrix and enables efficient tensor-product quadrature, which simplifies implementation and reduces memory bandwidth in explicit time stepping. Second, for shock-dominated multicomponent flows, $\mathbb{Q}^p$ bases provide enhanced numerical stability and more effective limiter performance due to their separable structure in each coordinate direction. Quantitative convergence tests (see Table 1) indicate that for $p = 3$, the $\mathbb{Q}^p$ basis achieves nearly identical L_2 accuracy to $\mathbb{P}^p$ with only about 10% additional computational cost, while exhibiting better conditioning and robustness near discontinuities. This choice therefore offers a favorable compromise between computational cost, accuracy, and stability for the mixed LDG framework applied to compressible multicomponent flows.

Table 1. Convergence study for 1D linear advection problem at $T_f = 1$. Here, e_2 and e_∞ denote the L_2 and L_∞ errors, respectively, and "O" represents the observed order of accuracy.

p	N	e_2	O	e_∞	O
1	24	6.8961×10^{-2}	–	4.2047×10^{-2}	–
	48	1.7582×10^{-2}	1.97	1.0509×10^{-2}	2.00
	96	4.4358×10^{-3}	1.99	2.6291×10^{-3}	2.00
	192	1.1239×10^{-3}	1.98	6.5804×10^{-4}	2.00
2	24	1.0134×10^{-3}	–	1.2293×10^{-3}	–
	48	1.2914×10^{-4}	2.97	1.5569×10^{-4}	2.98
	96	1.6325×10^{-5}	2.99	1.9643×10^{-5}	2.99
	192	2.0441×10^{-6}	2.99	2.4567×10^{-6}	3.00
3	24	1.7558×10^{-4}	–	2.6483×10^{-4}	–
	48	1.0951×10^{-5}	4.00	1.6527×10^{-5}	4.00
	96	6.8488×10^{-7}	4.00	1.0334×10^{-6}	4.00
	192	4.2838×10^{-8}	4.00	6.4601×10^{-8}	4.00
4	24	2.6375×10^{-6}	–	4.3171×10^{-6}	–
	48	8.0798×10^{-8}	5.03	1.3427×10^{-7}	5.00
	96	2.5098×10^{-9}	5.01	4.2113×10^{-9}	4.99
	192	7.7805×10^{-11}	5.01	1.3059×10^{-10}	5.01

3.3. Weak formulation

Having introduced the discrete approximation space, we now derive the weak formulation of Eq (3.1). To this end, we multiply Eq (3.1) by a test function $\phi_h \in \mathcal{V}_h^p$, integrate over an arbitrary element $m \subset \Omega_h$, and apply integration by parts. This yields

$$\begin{aligned}
&\int_m \mathbf{G}_h\,\phi_h\,dV + \int_m \nabla\phi_h\cdot\mathbf{U}_h\,dV - \int_e \phi_h\,\mathbf{U}_h\cdot\mathbf{n}\,dS = 0,\\
&\frac{\partial}{\partial t}\int_m \mathbf{U}_h\,\phi_h\,dV - \int_m \nabla\phi_h\cdot\mathbf{F}_{\mathrm{c}}(\mathbf{U}_h)\,dV + \int_e \phi_h\,\mathbf{F}_{\mathrm{c}}(\mathbf{U}_h)\cdot\mathbf{n}\,dS\\
&-\int_m \nabla\phi_h\cdot\mathbf{F}_{\mathrm{d}}(\mathbf{U}_h,\mathbf{G}_h)\,dV + \int_e \phi_h\,\mathbf{F}_{\mathrm{d}}(\mathbf{U}_h,\mathbf{G}_h)\cdot\mathbf{n}\,dS = 0,
\end{aligned} \tag{3.5}$$

where $\mathbf{n}$ denotes the outward-pointing unit normal vector on the boundary of the element m. Since the discrete fields $(\mathbf{U}_h, \mathbf{G}_h)$ are piecewise defined and may exhibit jumps across element interfaces, the boundary fluxes $\mathbf{U}_h\cdot\mathbf{n}$, $\mathbf{F}_c\cdot\mathbf{n}$, and $\mathbf{F}_d\cdot\mathbf{n}$ are not uniquely defined at the interfaces. In order to obtain a consistent and well-posed formulation, the physical fluxes are replaced by single-valued numerical interface fluxes, denoted by $\widehat{\mathbf{F}}^{\mathrm{aux}}$, $\widehat{\mathbf{F}}^{\mathrm{conv}}$, and $\widehat{\mathbf{F}}^{\mathrm{diff}}$. By substituting the physical fluxes with their numerical counterparts, the resulting weak formulation can be written in the following form:

$$\begin{aligned}
&\int\limits_m \mathbf{G}_h\,\phi_h\,dV + \int\limits_m \nabla\phi_h\cdot\mathbf{U}_h\,dV - \int\limits_e \phi_h\,\widehat{\mathbf{F}}^{\mathrm{aux}}\,dS = 0,\\
&\frac{\partial}{\partial t}\int\limits_m \mathbf{U}_h\,\phi_h\,dV - \int\limits_m \nabla\phi_h\cdot\mathbf{F}_{\mathrm{c}}(\mathbf{U}_h)\,dV + \int\limits_e \phi_h\,\widehat{\mathbf{F}}^{\mathrm{conv}}\,dS\\
&-\int\limits_m \nabla\phi_h\cdot\mathbf{F}_{\mathrm{d}}(\mathbf{U}_h,\mathbf{G}_h)\,dV + \int\limits_e \phi_h\,\widehat{\mathbf{F}}^{\mathrm{diff}}\,dS = 0.
\end{aligned} \tag{3.6}$$

To approximate the integrals over elements and interfaces, we adopt Gauss-Legendre quadrature rules such that the quadrature nodes coincide with the interpolation points [32].

$$\int_m f(\mathbf{x})\,dV \approx \sum_{i,j=0}^{p} \omega_i\,\omega_j\,J_m^{ij}\,f(\mathbf{x}_m^{ij}), \qquad \int_e f(\mathbf{x})\,dS \approx \sum_{k=0}^{p} \omega_k\,J_e^k\,f(\mathbf{x}_e^k), \tag{3.7}$$

where $\omega_i, \omega_j > 0$ denote the Gauss-Legendre weights, $J_m^{ij} = J_m(\mathbf{x}_m^{ij}) = \left|\mathbf{x}_{m,\xi}(\xi^{ij})\right|$, and $J_e^k = \left|\mathbf{x}_{e,\xi}(\xi^k)\right|$ is the Jacobian on the element edge.

The weak formulation in Eq (3.6) is obtained from the integral conservation form of the governing equations. Owing to the use of single-valued numerical fluxes across inter-element boundaries, the mixed LDG scheme maintains discrete conservation of mass, momentum, and total energy. This property is inherent to the formulation, as the flux contributions to the adjacent elements cancel exactly, and is verified numerically in the benchmark tests presented in Section 4.

3.4. Treatment of convective and diffusive fluxes

In this study, the inter-element convective fluxes are computed using the Harten-Lax-van Leer contact (HLLC) approximate Riemann solver, which is specifically designed for compressible two-component flow systems [33]. The numerical flux is expressed as

$$\widehat{\mathbf{F}}^{\mathrm{conv}} = \frac{1 + sign(S^*)}{2}\mathbf{F}_L^* + \frac{1 - sign(S^*)}{2}\mathbf{F}_R^*, \tag{3.8}$$

where $\mathbf{F}_L^*$ and $\mathbf{F}_R^*$ represent the left and right intermediate fluxes, respectively, and S^* is the speed of the middle wave. These intermediate quantities are obtained from

$$\mathbf{F}_k^* = \mathbf{F}_k + S_k(\mathbf{U}_k^* - \mathbf{U}_k), \quad S^* = \frac{P_R - P_L + \rho_L u_L(S_L - u_L) - \rho_R u_R(S_R - u_R)}{\rho_L(S_L - u_L) - \rho_R(S_R - u_R)}, \quad k = L, R, \tag{3.9}$$

with the intermediate conservative state given by

$$\mathbf{U}_k^* = \frac{S_k - u_k}{S_k - S^*}\begin{bmatrix} (\rho)_k \\ (\rho u)_k \\ (\rho v)_k \\ (\rho E)_k + (S^* - u_k)\left(\rho_k S^* + \frac{P_k}{(S_k - u_k)}\right) \\ (\rho\phi)_k \end{bmatrix}. \tag{3.10}$$

The left and right wave speeds S_L and S_R are approximated by

$$\begin{aligned} &S_L = \min(S_L^*, 0), \quad S_R = \max(S_R^*, 0), \\ &S_L^* = \min(\bar{u} - \bar{c}, u_L - c_L), \quad S_R^* = \max(\bar{u} + \bar{c}, u_R + c_R), \\ &\bar{u} = \frac{\sqrt{\rho_L}u_L + \sqrt{\rho_R}u_R}{\sqrt{\rho_L} + \sqrt{\rho_R}}, \quad \bar{c}^2 = \frac{\sqrt{\rho_L}c_L^2 + \sqrt{\rho_R}c_R^2}{\sqrt{\rho_L} + \sqrt{\rho_R}} + \frac{1}{2}\frac{\sqrt{\rho_L}\sqrt{\rho_R}}{(\sqrt{\rho_L} + \sqrt{\rho_R})^2}(u_R - u_L)^2. \end{aligned} \tag{3.11}$$

Additionally, the diffusive and auxiliary numerical fluxes are evaluated using the alternating flux strategy introduced in [30]. The corresponding numerical fluxes are defined as

$$\widehat{\mathbf{F}}^{\text{aux}} = \{\!\{\mathbf{U}_h\}\!\} - \widehat{\boldsymbol{\beta}} \cdot [\![\mathbf{U}_h]\!], \qquad \widehat{\mathbf{F}}^{\text{diff}} = \{\!\{\mathbf{F}(\mathbf{U}_h, \boldsymbol{\Theta}_h)\}\!\} + \widehat{\boldsymbol{\beta}} \cdot [\![\mathbf{U}_h]\!] - \tau\, [\![\boldsymbol{\Theta}_h]\!], \tag{3.12}$$

$$\widehat{\boldsymbol{\beta}} = \pm\tfrac{1}{2}\mathbf{n}, \qquad \tau \geq 0.$$

Here, $\{\!\{\cdot\}\!\}$ denotes the arithmetic average across the element interface, and $[\![\cdot]\!]$ represents the jump between the left and right states. The parameter $\tau \geq 0$ introduces optional stabilization. Following the LDG alternating-flux formulation [30], the choice $\widehat{\boldsymbol{\beta}} = \pm\frac{1}{2}\mathbf{n}$ provides alternating upwinding for the two components along the interface, while $\tau = 0$ yields the canonical alternating flux. The flux reduces to the central form when $\widehat{\boldsymbol{\beta}} = \mathbf{0}$ and $\tau = 0$.

3.5. High-order moment limiting strategy

To eliminate nonphysical oscillations in the vicinity of shocks and material interfaces without sacrificing high-order accuracy, a moment-based limiter [34] is applied. This limiter operates directly on the modal coefficients, starting from the highest-order mode and proceeding to lower modes only if the preceding one has been modified.

Let (k, m) denote a generic element and $\mathbf{U}_{i,j}^{k,m}$ the corresponding modal expansion coefficient. The limited value $\widetilde{\mathbf{U}}_{i,j}^{k,m}$ is evaluated by means of the following minmod-based formula:

$$\begin{aligned} \widetilde{\mathbf{U}}_{i,j}^{k,m} = \operatorname{minmod}(&\mathbf{U}_{i,j}^{k,m},\ \alpha_j(\mathbf{U}_{i,j-1}^{k,m+1} - \mathbf{U}_{i,j-1}^{k,m}),\ \alpha_j(\mathbf{U}_{i,j-1}^{k,m} - \mathbf{U}_{i,j-1}^{k,m-1}), \\ &\alpha_i(\mathbf{U}_{i-1,j}^{k+1,m} - \mathbf{U}_{i-1,j}^{k,m}),\ \alpha_i(\mathbf{U}_{i-1,j}^{k,m} - \mathbf{U}_{i-1,j}^{k-1,m})), \qquad 1 \leq i, j \leq N_l, \end{aligned} \tag{3.13}$$

where

$$\operatorname{minmod}(a,b,c) = \begin{cases} \operatorname{sgn}(a)\ \min(|a|,|b|,|c|), & \text{if } \operatorname{sgn}(a) = \operatorname{sgn}(b) = \operatorname{sgn}(c), \\ 0, & \text{otherwise.} \end{cases} \tag{3.14}$$

The parameters α_n act as tuning constants in the limiter and satisfy the bounds [34]

$$\frac{1}{2\sqrt{4n^2-1}} \ \leq\ \alpha_n \ \leq\ \sqrt{\frac{2n-1}{2n+1}}, \qquad n \in N_l. \tag{3.15}$$

In the numerical simulations reported in later sections, the values $\alpha_i = \alpha_j = 0.75$ are used, which were found to provide sufficient numerical dissipation without destroying the high-order resolution of the solution.

3.6. *Time integration*

Following spatial discretization, the mixed LDG formulation transforms the governing equations into a semi-discrete system of ordinary differential equations (ODEs), expressed as

$$\mathbf{M}\,\frac{d\mathbf{U}}{dt} = \mathbf{L}(\mathbf{U}), \tag{3.16}$$

where $\mathbf{M}$ denotes the block-diagonal mass matrix and $\mathbf{L}(\mathbf{U})$ represents the discrete residual of the spatial operator. Owing to the diagonal structure of $\mathbf{M}$, its inversion can be performed efficiently in an elementwise manner.

The temporal discretization of Eq (3.16) is achieved using the third-order strong-stability-preserving Runge-Kutta (SSP-RK3) scheme [35], defined as

$$\begin{aligned} \mathbf{U}^{(1)} &= \mathbf{U}^n + \Delta t\,\mathbf{L}(\mathbf{U}^n), \\ \mathbf{U}^{(2)} &= \tfrac{3}{4}\,\mathbf{U}^n + \tfrac{1}{4}\,\mathbf{U}^{(1)} + \tfrac{1}{4}\,\Delta t\,\mathbf{L}(\mathbf{U}^{(1)}), \\ \mathbf{U}^{n+1} &= \tfrac{1}{3}\,\mathbf{U}^n + \tfrac{2}{3}\,\mathbf{U}^{(2)} + \tfrac{2}{3}\,\Delta t\,\mathbf{L}(\mathbf{U}^{(2)}). \end{aligned} \tag{3.17}$$

The time step Δt is determined from the local CFL stability condition,

$$\Delta t = \frac{CFL}{2p+1}\,\frac{h}{|\lambda_{\max}^{\mathrm{inv}}| + 2\,|\lambda_{\max}^{\mathrm{vis}}|\left(\frac{2p+1}{h}\right)}, \tag{3.18}$$

where $h = \min(\Delta x, \Delta y)$ is the element size, CFL denotes the Courant-Friedrichs-Lewy number, and $\lambda_{\max}^{\mathrm{inv}}$ and $\lambda_{\max}^{\mathrm{vis}}$ are the largest eigenvalues of the inviscid and viscous flux Jacobians, respectively.

The SSP-RK3 method is selected for its excellent balance between accuracy, stability, and computational efficiency, making it well suited for nonlinear hyperbolic systems. It preserves the total variation diminishing (TVD) property of the forward Euler step under an appropriate CFL constraint, thereby preventing spurious oscillations near discontinuities and ensuring monotonicity preservation. The scheme achieves third-order temporal accuracy while maintaining strong stability properties, and it is widely employed with high-order methods for compressible flow problems involving shocks and sharp gradients. Compared with standard explicit Runge-Kutta or multistep methods, SSP-RK3 provides superior numerical robustness and stability at a moderate computational cost, offering an optimal compromise for the present simulations.

4. Simulation results and analysis

In this section, a series of benchmark problems are presented to demonstrate the robustness and accuracy of the proposed mixed LDG scheme. Following a convergence study, both 1D and 2D shock-interface configurations are investigated to illustrate the capability of the scheme in capturing shock-driven instabilities in multicomponent flows. Unless otherwise stated, a polynomial order of $p = 3$ is employed for all test cases, which provides an optimal balance between accuracy and computational cost as verified in the convergence study (Table 1).

4.1. 1D accuracy verification

As a first step, we evaluate the spatial accuracy of the proposed mixed LDG discretization using a 1D linear advection problem,

$$\frac{\partial u}{\partial t} + \frac{\partial u}{\partial x} = 0, \qquad x \in [0,\, 2\pi], \tag{4.1}$$

supplemented with the periodic condition $u(0, t) = u(2\pi, t)$ and the initial profile $u(x, 0) = \sin(x)$. The corresponding analytical solution is $u_{\mathrm{ex}}(x, t) = \sin(x - t)$. The test is carried out using polynomial degrees $p = 1, 2, 3, 4$ on successively refined meshes ($N = 24, 48, 96, 192$), and the numerical errors are evaluated at the final time $T_f = 1$. For each grid, the discretization errors in the L_∞ and L_2 norms are determined as follows:

$$e_\infty = \max_{x\in[0,\,2\pi]} |u_{\mathrm{ex}}(x, t) - u_h(x, t)|, \qquad e_2 = \Big(\sum_{I_n} \int_{I_n} |u_{\mathrm{ex}}(x, t) - u_h(x, t)|^2\, dx\Big)^{1/2}, \tag{4.2}$$

The errors and corresponding convergence rates are listed in Table 1. The results clearly confirm that the present mixed LDG scheme exhibits an order of convergence equal to $(p + 1)$ in both norms, which is consistent with the theoretical prediction.

The temporal accuracy of the third-order SSP-RK3 scheme was verified using the same 1D linear advection problem on an over-resolved grid to suppress spatial errors. The errors and rates listed in Table 2 confirm third-order temporal convergence, consistent with the theoretical accuracy of the SSP-RK3 integrator.

Table 2. Temporal convergence of the SSP-RK3 time-integration scheme for 1D linear advection problem, confirming third-order accuracy.

Time step Δt	e_2	O
1.0×10^{-2}	1.26×10^{-5}	–
5.0×10^{-3}	1.55×10^{-6}	3.02
2.5×10^{-3}	1.91×10^{-7}	3.02
1.25×10^{-3}	2.38×10^{-8}	3.01

4.2. 2D accuracy verification

To further assess the spatial accuracy of the proposed mixed LDG scheme in multiple dimensions, we consider a two-dimensional linear advection equation,

$$\frac{\partial u}{\partial t} + a\frac{\partial u}{\partial x} + b\frac{\partial u}{\partial y} = 0, \quad (x, y) \in [0, 2] \times [0, 2], \tag{4.3}$$

subject to periodic boundary conditions in both directions. The advection coefficients are taken as $a = b = 1$, and the initial condition is specified as

$$u(x, y, 0) = \sin[\pi(x + y)]. \tag{4.4}$$

The analytical solution of this problem is given by

$$u_{\text{ex}}(x, y, t) = \sin[\pi(x - at + y - bt)]. \tag{4.5}$$

This problem represents smooth periodic transport along the diagonal direction and serves as a suitable benchmark for verifying the multidimensional accuracy of the scheme. The test is performed using polynomial degrees $p = 1, 2, 3$ on a sequence of successively refined uniform meshes with $N_x \times N_y = 10^2, 20^2, 40^2, 80^2$, and 160^2 elements. The final simulation time is set to $T_f = 1$.

Figure 1(a,b) presents the contour and surface plots of the computed solution using a third-order mixed LDG scheme on a 20×20 mesh, which demonstrates smooth and non-oscillatory transport. Figure 1(c) compares the numerical and analytical profiles extracted along the diagonal line of the computational domain, showing excellent agreement and confirming the high-resolution capability of the proposed method.

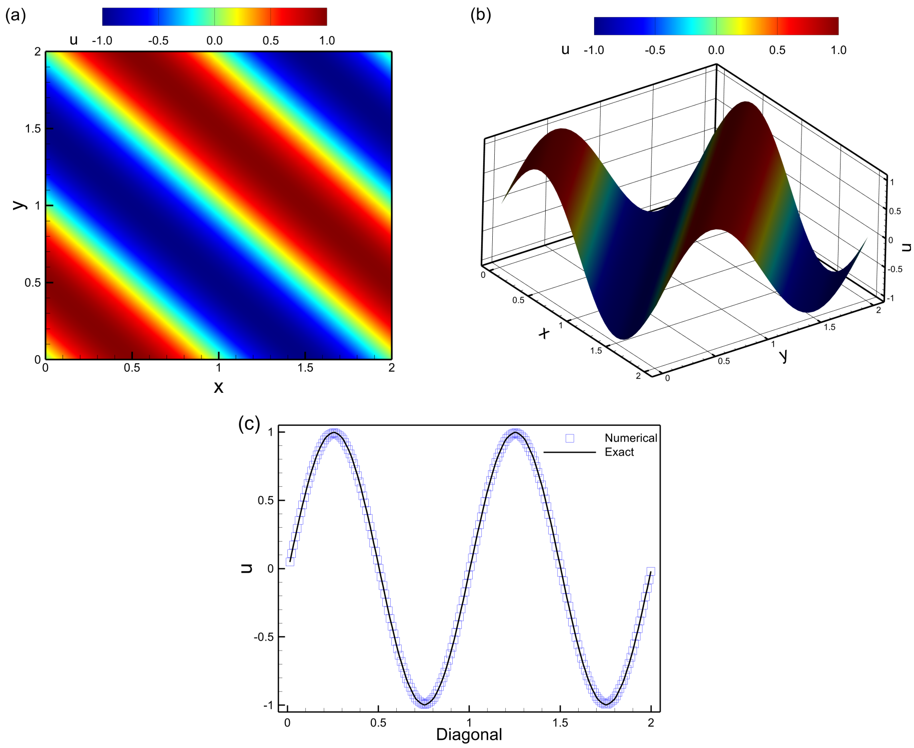

Figure 1. 2D linear advection problem: (a) contour plot of the solution field, (b) corresponding surface representation, and (c) comparison of the numerical LDG solution with the analytical profile along the diagonal direction using 20×20 mesh at $T_f = 1$.

To quantitatively assess the convergence behavior, the discrete L_∞ and L_2 errors are computed between the exact and numerical solutions using sufficiently accurate Gaussian quadrature rules,

$$e_\infty = \max_{(x,y)\in\Omega} |u_{\text{ex}}(x, y, t) - u_h(x, y, t)|, \quad e_2 = \left(\sum_K \int_K |u_{\text{ex}}(x, y, t) - u_h(x, y, t)|^2 \, d\Omega \right)^{1/2}. \tag{4.6}$$

The corresponding errors and observed orders of accuracy are listed in Table 3, and their variation with respect to the number of elements and degrees of freedom (DoF) is illustrated in Figure 2. The results clearly demonstrate that the present mixed LDG scheme achieves the optimal convergence rate of $(p + 1)$ in both L_2 and L_∞ norms for all tested polynomial degrees. This confirms the expected theoretical accuracy and validates the robustness and multidimensional consistency of the proposed formulation for smooth transport problems.

Table 3. Convergence study for 2D linear advection problem at $T_f = 1$.

p	$N_x \times N_y$	DoF	e_∞	O	e_2	O
1	10^2	$10^2 \times 4$	$5.98E-02$	–	$4.11E-02$	–
	20^2	$20^2 \times 4$	$1.53E-02$	1.97	$1.03E-02$	2.00
	40^2	$40^2 \times 4$	$3.60E-03$	2.08	$2.50E-03$	2.04
	80^2	$80^2 \times 4$	$8.57E-04$	2.07	$6.02E-04$	2.05
	160^2	$160^2 \times 4$	$1.93E-04$	2.15	$1.34E-04$	2.17
2	10^2	$10^2 \times 9$	$2.67E-03$	–	$2.75E-03$	–
	20^2	$20^2 \times 9$	$3.43E-04$	2.96	$3.54E-04$	2.95
	40^2	$40^2 \times 9$	$4.54E-05$	2.91	$4.42E-05$	3.00
	80^2	$80^2 \times 9$	$5.63E-06$	3.01	$5.53E-06$	2.99
	160^2	$160^2 \times 9$	$6.54E-07$	3.11	$6.91E-07$	3.00
3	10^2	$10^2 \times 16$	$6.04E-04$	–	$5.97E-04$	–
	20^2	$20^2 \times 16$	$3.72E-05$	4.02	$3.88E-05$	3.94
	40^2	$40^2 \times 16$	$2.66E-06$	3.81	$2.57E-06$	3.92
	80^2	$80^2 \times 16$	$1.81E-07$	3.88	$1.91E-07$	3.75
	160^2	$160^2 \times 16$	$1.17E-08$	3.92	$1.21E-08$	3.98

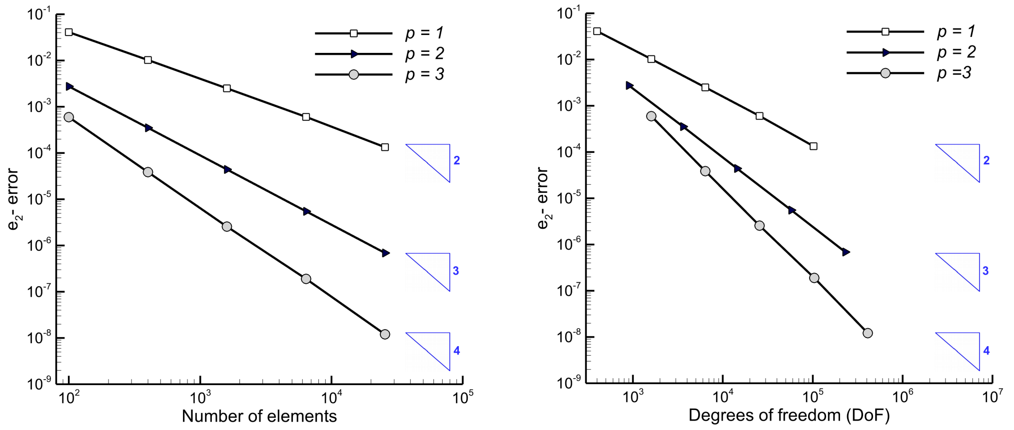

Figure 2. Convergence analysis for 2D linear advection problem: variation of the L_2-norm error (e_2) with (a) the number of elements and (b) the total DoF for polynomial orders $p = 1, 2$, and 3.

4.3. 1D Sod shock tube

To evaluate the performance of the proposed mixed LDG solver in handling discontinuities and accurately modeling shock-interface interactions, we first consider the classical 1D Sod shock tube problem. This problem represents a two-component Riemann problem governed by 1D compressible Euler equations, and is widely used as a standard benchmark for shock-capturing methods.

The computational domain is defined as $\Omega_D = [0,1]$, with the initial discontinuity positioned at $x = 0.5$. The left and right states are specified as follows [4]:

$$(\rho, u, p, \gamma) = \begin{cases} (1.0, 0.0, 1.0, 1.4), & x \leq 0.5, \\ (0.125, 0.0, 0.1, 1.6), & x \geq 0.5. \end{cases} \tag{4.7}$$

The simulation is performed using 400 grid points. From these initial data, a right-moving shock, a left-going rarefaction, and a contact discontinuity are generated. The key numerical parameters employed for this test case, including the polynomial order, grid resolution, time-integration details, and boundary conditions, are summarized in Table 4.

Table 4. Simulation parameters for 1D Sod shock tube problem.

Parameter	**Symbol/description**	**Value**
Polynomial order	p	3
Grid resolution	N_x	400 grid points
Domain size	Ω_D	[0, 1]]
Time integration	SSP-RK3	$CLF = 0.2$
Left/right states	$(\rho, u, p, \gamma)_L$, $(\rho, u, p, \gamma)_R$	(1.0, 0, 1.0, 1.4); (0.125, 0, 0.1, 1.6)
Boundary conditions	–	Fixed inflow/outflow
Final time	T_f	0.25

Figure 3 shows the numerical results at $t = 0.25$ for the density and pressure profiles, together with the analytical solution. The numerical and exact solutions agree very well, confirming the ability of the present method to accurately capture all relevant wave structures without introducing spurious oscillations. For visualization, the mixed LDG solution is sampled at element centers (cell-averaged values).

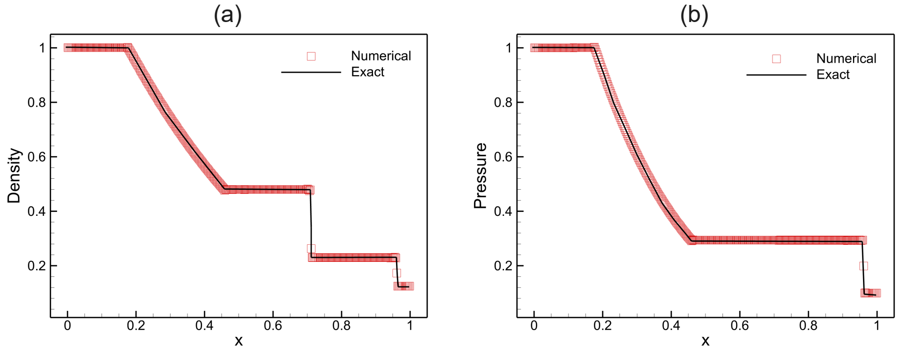

Figure 3. Density and pressure profiles obtained for the 1D Sod shock tube at $t = 0.25$. Symbols correspond to the mixed LDG solution sampled at element centers, while the solid line indicates the exact analytical result.

To further verify the conservative nature of the proposed mixed LDG formulation, we evaluated the global conservation of mass, momentum, and total energy for the 1D Sod shock-tube test. The integral quantities were computed at each time step as

$$M(t) = \int_{\Omega} \rho \, dx, \qquad P(t) = \int_{\Omega} \rho u \, dx, \qquad E(t) = \int_{\Omega} \rho E \, dx, \tag{4.8}$$

and the relative conservation errors were defined as

$$\varepsilon_M = \frac{|M(t) - M(0)|}{M(0)}, \qquad \varepsilon_P = \frac{|P(t) - P(0)|}{|P(0)| + 10^{-12}}, \qquad \varepsilon_E = \frac{|E(t) - E(0)|}{E(0)}. \tag{4.9}$$

For a representative grid of $N = 400$ grid points and polynomial degree $p = 3$, the obtained errors at $t = 0.25$ were $\varepsilon_M = 2.3 \times 10^{-13}$, $\varepsilon_P = 4.1 \times 10^{-12}$, and $\varepsilon_E = 5.7 \times 10^{-13}$. These results confirm that the mixed LDG scheme preserves the global conservation of mass, momentum, and total energy to within machine precision, consistent with the conservative formulation of Eqs (3.6), (3.8), and (3.12). Table 5 further confirms that the proposed mixed LDG formulation retains discrete conservation of mass, momentum, and energy for all tested polynomial orders.

Table 5. Conservation errors of mass (ε_M), momentum (ε_P), and energy (ε_E) for 1D Sod shock-tube test at $t = 0.25$.

Polynomial order p	ε_M	ε_P	ε_E
1	4.7×10^{-12}	6.3×10^{-11}	8.2×10^{-12}
2	1.9×10^{-13}	2.5×10^{-12}	3.2×10^{-13}
3	2.3×10^{-13}	4.1×10^{-12}	5.7×10^{-13}
4	1.5×10^{-14}	3.6×10^{-13}	2.2×10^{-14}

4.4. 2D shock-driven heavy cylindrical interface

As a second benchmark, we consider the classical 2D shock-driven heavy cylindrical interface, in which a planar shock wave interacts with a heavy cylindrical gas interface. The experimental data of Hass and Sturtevant [36] and the numerical results of Quirk and Karni [37] are used for validation and comparison. In these studies, the bubble consists of Refrigerant-22 (R_{22}) surrounded by air, and is impulsively accelerated by a weak incident shock of Mach number $M_s = 1.22$. The numerical setup and boundary conditions adopted for this benchmark are summarized in Table 6. These parameters closely follow the configurations of Hass and Sturtevant [36] and Quirk and Karni [37], ensuring direct comparability between the present simulations and reference data.

Table 6. Simulation parameters for 2D shock-driven heavy cylindrical interface.

Parameter	**Symbol/description**	**Value**
Gas composition	–	Air/R_{22}
Incident shock Mach number	M_s	1.22
Polynomial order	p	3
Grid resolution	$N_x \times N_y$	1200×600 cells
Domain size	–	$[0,\ 890] \times [0,\ 89]$ mm^2
Time integration	SSP-RK3	$CLF = 0.1$
Boundary conditions	–	left - inflow; others - non-reflecting

Figure 4 compares Schlieren images at different physical times (55μs, 98μs, 147μs, 197μs and 247μs) obtained from the experiments, reference simulations, and the present LDG scheme. At t = 55μs, the incident shock reaches the upstream side of the cylindrical interface and undergoes reflection and refraction as it passes through the density discontinuity. At t = 98μs, the transmitted shock propagates inside the dense bubble, while a reflected shock travels back into the ambient region and the interface starts to distort. Afterwards, at t = 147μs, the density contrast triggers baroclinic vorticity and a downstream jet begins to form. By t = 197μs, strong shear layers develop, and vortex roll-up occurs along the interface. Finally, at t = 247μs, well-developed vortical structures are observed, together with continued jet penetration. The present mixed LDG solution faithfully reproduces these essential physical mechanisms, including the jet penetration, shock refraction, and vortex roll-up.

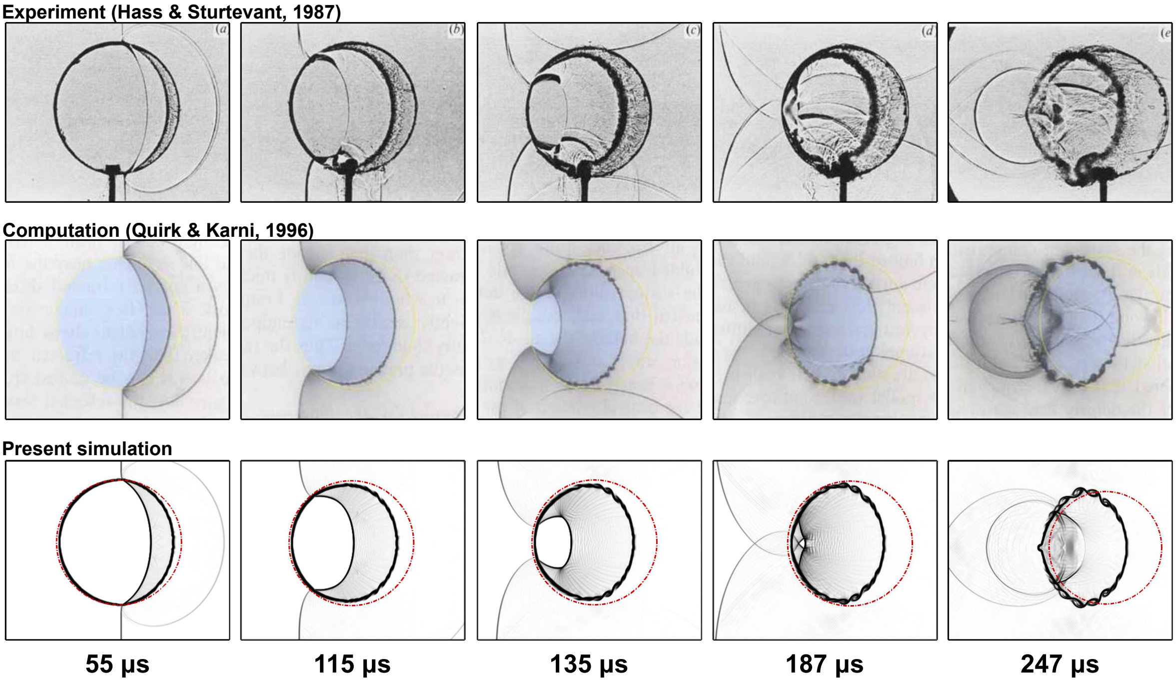

Figure 4. Schlieren comparison of the experimental data [36], reference computation [37], and present LDG simulation of a 2D shock-driven heavy cylindrical interface at successive times (55–247μs).

To evaluate the predictive capability quantitatively, Figure 5 depicts the evolution of several characteristic interface and shock fronts, namely the incident shock (IS), reflected shock (RS), transmitted shock (TS), upstream interface (UI), and downstream interface (DI). The numerical trajectories show very good agreement with the experimental measurements in terms of both location and propagation speed. This confirms that the proposed LDG formulation can accurately capture the shock-interface interaction dynamics and the complex flow evolution triggered by baroclinic vorticity generation.

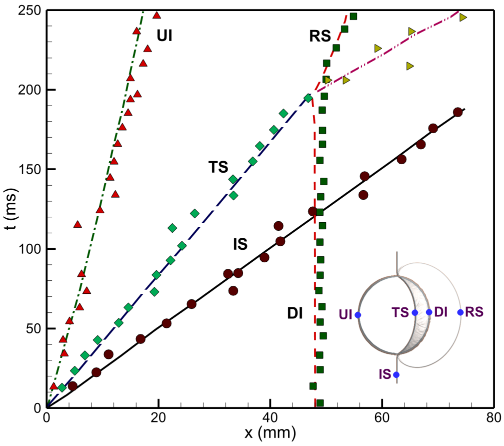

Figure 5. Comparison of the characteristic interface trajectories (IS, UI, DI, TS, RS) for a 2D shock-driven heavy cylindrical interface: experimental data [36] versus present mixed LDG simulation. Symbols denote experimental measurements, while lines indicate the corresponding numerical predictions.

4.5. 2D shock-driven light cylindrical interface

For the next benchmark, we consider the classical 2D shock-driven light cylindrical interface, in which a planar shock wave interacts with a helium cylindrical gas region embedded in air. The experimental data of Haas and Sturtevant [36] and the numerical results of Quirk and Karni [37] are used for validation and comparison. The simulation setup, including gas composition, grid resolution, domain size, and boundary conditions, is summarized in Table 7. These parameters are chosen to ensure close agreement with the reference configurations and to facilitate a direct comparison of interface deformation and shock refraction dynamics.

Table 7. Simulation parameters for 2D shock-driven heavy cylindrical interface.

Parameter	**Symbol/description**	**Value**
Gas composition	–	Air/He
Incident shock Mach number	M_s	1.22
Polynomial order	p	3
Grid resolution	$N_x \times N_y$	1200×600 cells
Domain size	–	$[0,\ 890] \times [0,\ 89]$ mm^2
Time integration	SSP-RK3	$CLF = 0.1$
Boundary conditions	–	left - inflow; others - non-reflecting

Figure 6 compares the present mixed LDG simulation against the experimental Schlieren images of Haas and Sturtevant [36] and the reference computation of Quirk and Karni [37]. This canonical test case is widely used to assess the ability of numerical schemes to capture shock-light-gas interactions, and therefore serves as an important validation prior to investigating the complex interface configuration. At the early times $t = 32\mu$s and 62μs, the incident shock impinges on the helium cylinder and produces a transmitted shock inside the light gas, a reflected shock propagating upstream, and an initially smooth contact surface that starts to deform due to baroclinic vorticity deposition at the curved density interface. By $t = 82\mu$s, the interface is elongated in the streamwise (shock-normal) direction, and a distinct roll-up can be observed at the cylinder edges. At $t = 102\mu$s, well-defined vortex pairs form along the flanks of the interface as a result of KH shear instabilities. Finally, at $t = 245\mu$s, the interface exhibits pronounced deformation and small-scale structures, accompanied by secondary wave interactions and enhanced mixing. The agreement between the present simulation and the reference datasets is very good in terms of both the timing and morphology of the transmitted and reflected shock waves, the development of the vortex pairs, and the overall interface evolution.

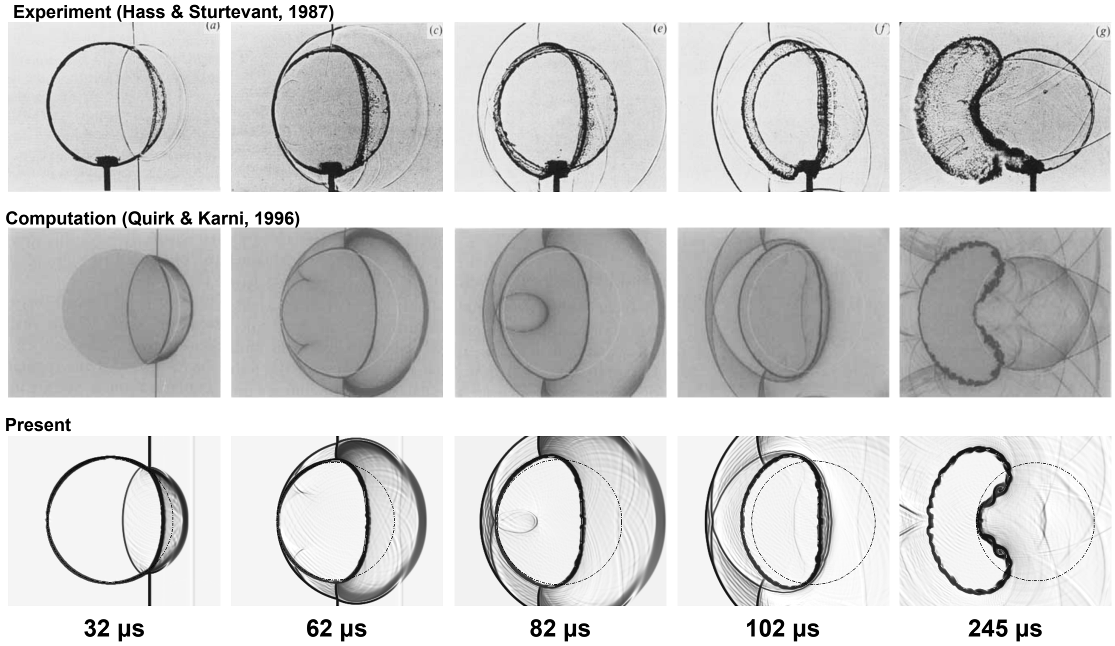

Figure 6. Schlieren comparison of the experimental data [36], reference computation [37], and present mixed LDG simulation of a 2D shock-driven light cylindrical interface at successive times (32–245μs).

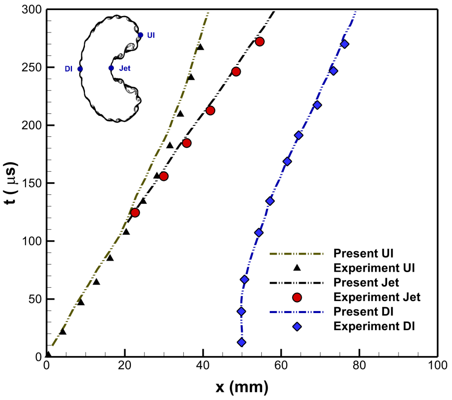

Figure 7. Comparison of the characteristic interface trajectories (UI, DI, Jet) for a 2D shock-driven light cylindrical interface: experimental data [36] versus present mixed LDG simulation. Symbols denote experimental measurements, while lines indicate the corresponding numerical predictions.

Figure 7 provides a quantitative assessment of the solver performance by tracking the characteristic interface locations; namely, the UI, DI, and the jet tip. The *t*-*x* trajectories extracted from the present simulation are compared with experimental measurements [36], with the symbols indicating experimental data and the lines showing the numerical predictions. The good agreement in both the slopes and the overall trend of the trajectories demonstrates that the present solver can accurately predict the interface acceleration, deformation rate, and jet penetration distance triggered by the shock.

4.6. 2D shock-driven heavy chevron interface

Following the cylindrical interface benchmarks, we consider a 2D shock interaction with a heavy chevron-shaped interface as an additional validation problem. Table 8 provides a concise overview of the simulation configuration, detailing the gas mixture, grid resolution, computational domain, and boundary conditions. This configuration introduces sharp interface corrugations, which enhance baroclinic vorticity generation and therefore provide a demanding test of the solver's ability to capture shock-induced mixing.

Table 8. Simulation parameters for the shock-driven heavy chevron interface.

Parameter	Symbol/description	Value
Gas composition	–	Air/SF_6
Incident shock Mach number	M_s	1.20
Vertex angle	θ	60°
Polynomial order	p	3
Grid resolution	$N_x \times N_y$	1200×600 cells
Domain size	–	$[0,\ 310] \times [0,\ 155]$ mm^2
Time integration	SSP-RK3	$CFL = 0.1$
Boundary conditions	–	left - inflow; Others - non-reflecting

The present numerical results are compared with the experiments of Luo et al. [38], who investigated a 2D shock-driven chevron-shaped air/SF_6 interface subjected to a planar shock of Mach number M_s = 1.2 and a vertex angle of θ = 60°.

Figure 8(a) shows a comparison of the Schlieren images at several time instants (t = 64μs, 171μs, 408μs, 531μs, and 1011μs). Immediately after shock impact (t = 64μs), the incident wave is partially transmitted into the heavier SF_6 gas and partially reflected back into the air region, resulting in a curved transmitted shock front and a reflected compression wave. Because of the strong density gradient across the chevron interface, a significant baroclinic vorticity is generated, and the interface tips start to bend and lose their original symmetry. In the intermediate stages (171–408μs), the baroclinic torque amplifies the corrugations and drives the formation of elongated jets at the chevron apex, while secondary compression and shear waves emanate from the interface corners. At later times (531–1011μs), the jet structures merge and roll up into large vortex cores and fine-scale vortical filaments, accompanied by the interaction of transmitted, reflected, and re-reflected waves. The Schlieren patterns predicted by the present scheme closely match those observed experimentally and capture the key physical processes such as shock refraction, jet growth, vortex roll-up, and secondary wave generation. Figure 8(b) provides a quantitative comparison by showing the temporal evolution of the upstream interface displacement D_s. The experimental measurements are plotted by symbols, while the corresponding numerical predictions are shown by solid lines. The close agreement over the full evolution interval confirms the ability of the present mixed LDG scheme to accurately reproduce both large-scale interface motion and the associated small-scale flow features.

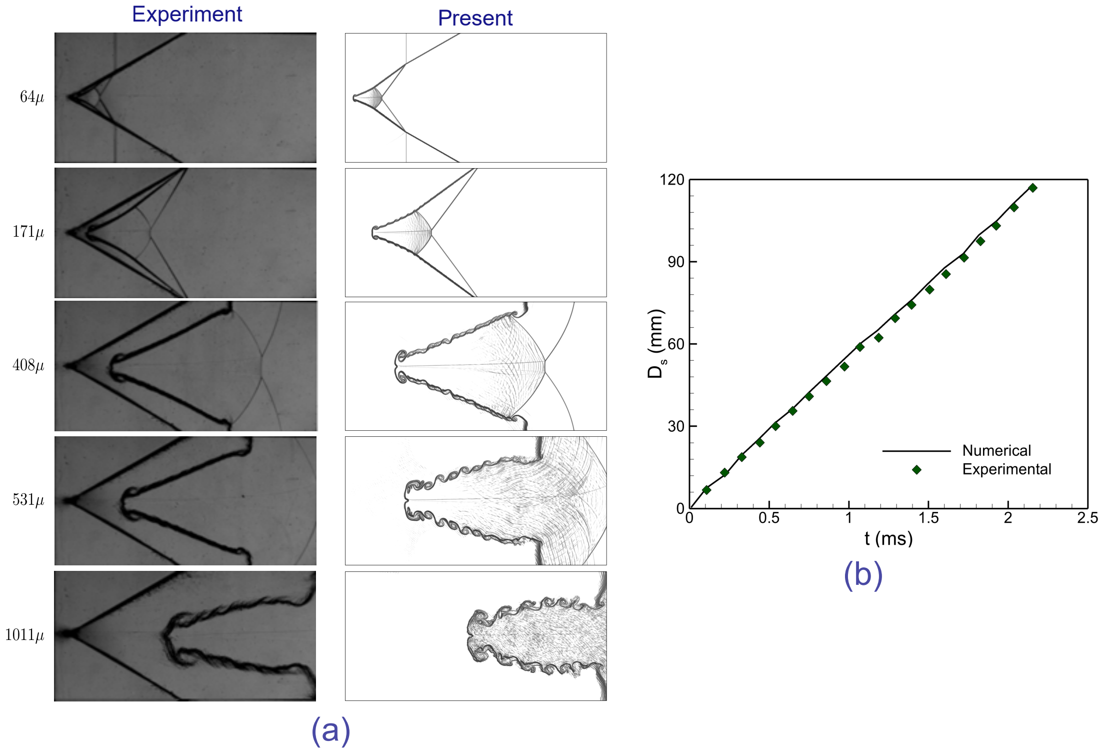

Figure 8. Comparison of the present mixed LDG simulation with 2D chevron-shaped shock-interface experiment of Luo et al. [38] at $M_s = 1.2$ and a vertex angle of 60°: (a) numerical and experimental Schlieren images at selected times ($t = 64\mu$s, 171μs, 408μs, 531μs, and 1011μs); (b) evolution of the upstream interface displacement, with symbols representing experimental data and the solid line indicating the numerical prediction.

4.7. 2D shock-driven single-mode heavy fluid layer

As a final test case, we examine the interaction of a planar shock wave with a 2D single-mode heavy fluid layer. This classical RM configuration features a sinusoidally perturbed interface and allows us to evaluate the ability of the mixed LDG scheme to capture shock-induced modal growth, vortex formation, and the transition to nonlinear deformation [39, 40].

Figure 9 shows the initial setup adopted for a 2D shock-driven single-mode heavy fluid layer configuration. The computational domain extends over 200mm in the streamwise (x) direction and 100mm in the transverse (y) direction. A layer of helium of base thickness d is placed inside the domain and is bounded by two material interfaces: an upstream interface I_1 that has a sinusoidal perturbation, and a downstream interface I_2 that is initially flat. The upstream interface is defined using a sinusoidal wave of amplitude a_0 and wavelength $\lambda = 100$mm, resulting in a maximum local layer thickness of $d + a_0/2$. The incident shock (initially located 25mm from the left boundary) travels from left to right and meets the perturbed interface I_1, the leftmost point of which is placed 5mm downstream of the shock. A set of simulations is carried out to examine the effect of selected geometric and flow parameters. Specifically, two SF_6 layer thicknesses ($d = 5$ and 40mm) are investigated using a fixed perturbation amplitude of $a_0 = 15$mm and an incident shock Mach number of $M_s = 1.25$. The key numerical parameters adopted for this case, including the Mach number, grid resolution, layer thickness, and time-integration details, are summarized in Table 9. These settings are selected to replicate the classical single-mode RM configuration and to ensure adequate resolution of interface deformation and vortex dynamics throughout the simulation. The relevant physical properties of SF_6 and the surrounding N_2 are listed in Table 10.

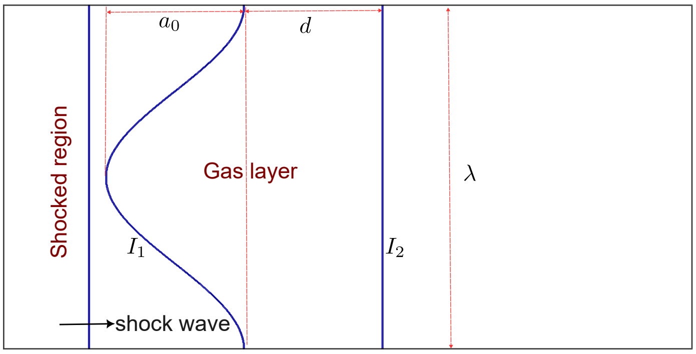

Figure 9. Schematic of the initial configuration for a 2D shock-driven single-mode heavy fluid layer. A planar shock propagates from left to right and interacts with a heavy fluid layer of thickness d, bounded by a sinusoidally perturbed upstream interface I_1 (initial amplitude a_0, wavelength λ) and a planar downstream interface I_2.

Table 9. Simulation parameters for a 2D single-mode heavy fluid layer.

Parameter	**Symbol/description**	**Value**
Gas composition	–	N_2/SF_6
Incident shock Mach number	M_s	1.25
Wavelength	λ	100mm
Initial amplitude	a_0	15mm
Layer thickness	d	5, and 40mm
Polynomial order	p	3
Grid resolution	$N_x \times N_y$	1200×600 cells
Domain size	–	$[0,\ 200] \times [0,\ 100]\ \mathrm{mm}^2$
Time integration	SSP-RK3	$CFL = 0.10$
Boundary conditions	–	left - inflow; Others - non-reflecting

Table 10. Used gas parameters for the numerical calculations.

Gas	Heat ratio (γ)	Density ($\mathrm{g \cdot cm^{-3}}$)	Specific heat ($\mathrm{kJ \cdot g^{-1} \cdot K^{-1}}$)	Molecular weight ($\mathrm{g \cdot mol^{-1}}$)
N_2	1.40	1.25×10^{-3}	1.04×10^{-3}	28.0134
SF_6	1.09	6.03×10^{-3}	0.656×10^{-3}	128.491

To prevent artificial wave reflections, an inflow boundary condition is imposed on the left side of the domain, an outflow boundary condition on the right side, and non-reflecting open boundary conditions on the top and bottom boundaries. All simulations start from a quiescent ambient state with $P_0 = 101{,}325$Pa and $T_0 = 293$K. For clarity in the subsequent analysis, the temporal evolution of the flow is expressed in terms of a nondimensional time scale. The physical time t is nondimensionalized using a characteristic time $t_0 = L/V_i$, where L denotes the wavelength of the perturbed interface and V_i is the velocity of the incident shock. The resulting dimensionless time is therefore defined as $\tau = t/t_0 = tV_i/L$.

To ensure the numerical accuracy and stability of the present simulations, a systematic grid-resolution study was conducted for the 2D shock-driven single-mode heavy fluid layer at $M_s = 1.25$. The flow evolution was examined on four uniform Cartesian grids: Grid-I (200 × 100), Grid-II (400 × 200), Grid-III (800 × 400), and Grid-IV (1200 × 600). The non-dimensional time is defined as $\tau = tU_s/\lambda$, where U_s is the shock velocity and λ denotes the perturbation wavelength.

Figure 10 presents the instantaneous density contours at $\tau = 80$ for the four grid levels. On the coarsest grid (Grid-I), the contact discontinuity is diffused, and small-scale vortical structures are poorly resolved. Refinement to Grid-II yields a much sharper interface and accurately captures the formation of the primary vortex pair generated by baroclinic torque. Grid-III further improves the resolution of secondary vortices and interface undulations, revealing the detailed roll-up process. The finest grid (Grid-IV) provides additional small-scale features near the interface and within the shear layer, confirming that finer vortical structures continue to emerge at higher resolutions. Based on these observations, the 1200 × 600 grid was selected for subsequent simulations to ensure accurate representation of shock-interface interactions while maintaining computational efficiency.

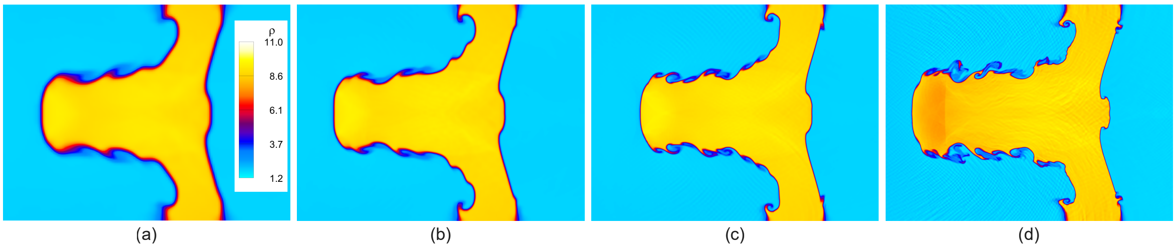

Figure 10. Density contours at $\tau = 80$ for 2D shock-driven single-mode heavy fluid layer, computed on four different grids: (a) Grid-I (200 × 100), (b) Grid-II (400 × 200), (c) Grid-III (800 × 400), and (d) Grid-IV (1200 × 600).

Figure 11 depicts the temporal evolution of the baroclinic vorticity magnitude $|\omega_{\text{bar}}|$ and the enstrophy Ω across the four grid resolutions. Both quantities exhibit a sharp initial rise immediately after shock impact, corresponding to impulsive vorticity deposition at the perturbed interface, followed by sustained growth due to vortex roll-up and secondary shear-layer interactions. The overall magnitude of both diagnostics increases consistently with grid refinement, indicating improved capture of small-scale vorticity and baroclinic torque effects. The finest grid (Grid-IV) shows significantly higher late-time amplification compared with the coarser grids, highlighting the importance of sufficient spatial resolution for resolving secondary vortices and fine-scale mixing. Consequently, the 1200×600 grid is adopted for all production runs to ensure accurate quantification of instability growth and vorticity dynamics.

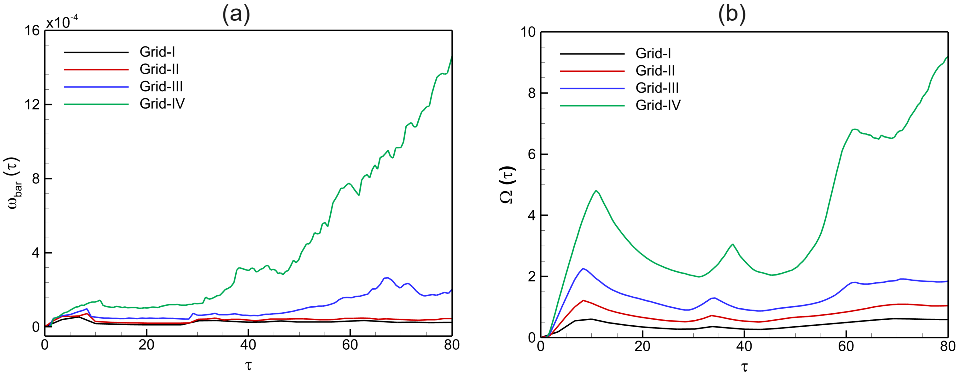

Figure 11. Temporal evolution of diagnostic quantities for 2D shock-driven single-mode heavy fluid layer, using four different grids: (a) baroclinic vorticity magnitude $|\omega_{\text{bar}}|$, and (b) enstrophy Ω.

Figure 12 illustrates the temporal evolution of the 2D shock-driven single-mode SF_6 layer for two different layer thicknesses. In both cases, the incident shock initially reaches the upstream sinusoidal interface, generating a transmitted wave inside the dense SF_6 layer and a reflected wave in the air. For the thin layer case (d = 5mm), as shown in Figure 12(a), the transmitted shock rapidly reaches the downstream (planar) interface and reflects back toward the upstream interface at an early time. This results in an immediate interaction between reflected waves and the evolving vortical structures, leading to the prompt formation of tightly spaced vortex pairs. As observed in the frames for τ = 40–80, the interface undergoes intense roll-up, and the vortices begin to merge, forming a complex mixing layer. In contrast, for the thicker layer (d = 40mm), as shown in Figure 12(b), the transmitted shock requires more time to reach the downstream interface. Consequently, the early-time interface evolution (τ = 0–30) is governed primarily by baroclinic vorticity deposition at the upstream interface, resulting in a slower growth of the modal perturbation. Only at later times ($\tau \geq 50$), once the transmitted and reflected waves begin to interact with the interface, more vigorous vortex roll-up develops. Compared to the thin-layer case, the vortical structures are more widely spaced and less fragmented, indicating that the larger separation between the interfaces delays nonlinear interaction and suppresses the formation of small-scale instabilities.

Figure 13 shows the time evolution of the vorticity field for the 2D shock-driven single-mode SF_6 layer with two different layer thicknesses. The vorticity is defined as the curl of the velocity field, $\boldsymbol{\omega} = \nabla \times \mathbf{u}$, which in two dimensions reduces to the scalar expression $\omega = \frac{\partial u_y}{\partial x} - \frac{\partial u_x}{\partial y}$. Large values of ω therefore indicate regions of intense local rotation associated with baroclinic vortex production at the interface. At early times (τ = 10 and 20), the vorticity is concentrated along the upstream sinusoidal interface and forms opposite-sign regions on either side of the perturbation, in accordance with the baroclinic source mechanism resulting from the misalignment of pressure and density gradients. For the thin layer case (d = 5mm), the transmitted shock quickly reaches the downstream interface and reflects back toward the upstream surface, which intensifies the vorticity magnitude and promotes early vortex roll-up (τ = 40). By τ = 80, multiple counter-rotating vortices have developed along the interface and secondary instabilities appear due to wave-vortex interactions. In the thicker layer (d = 40mm), the vorticity distribution remains smooth and coherent up to τ = 40, as the transmitted shock has not yet interacted with the downstream interface. Only at later times ($\tau \simeq 80$) does the reflected wave impinge on the upstream interface, and initiate more vigorous vortex roll-up. Compared to the thin-layer configuration, the vortices are more widely spaced and less fragmented, indicating that the increased layer thickness delays the onset of the nonlinear stage of the RM instability and reduces the production of small-scale vortical structures.

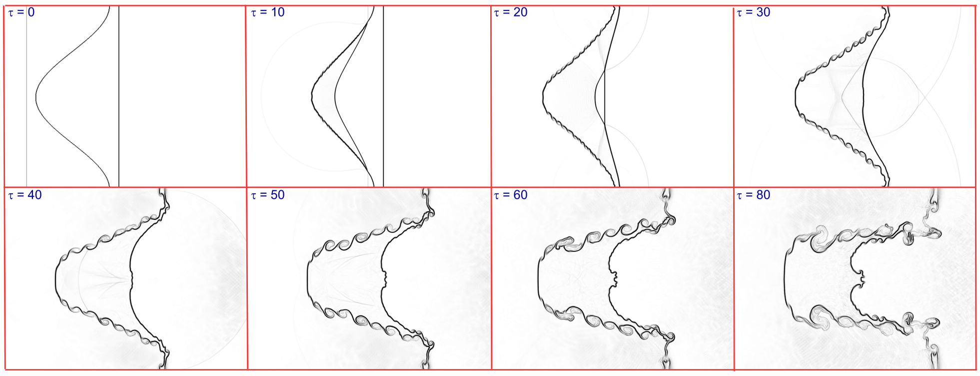

(a) d = 5

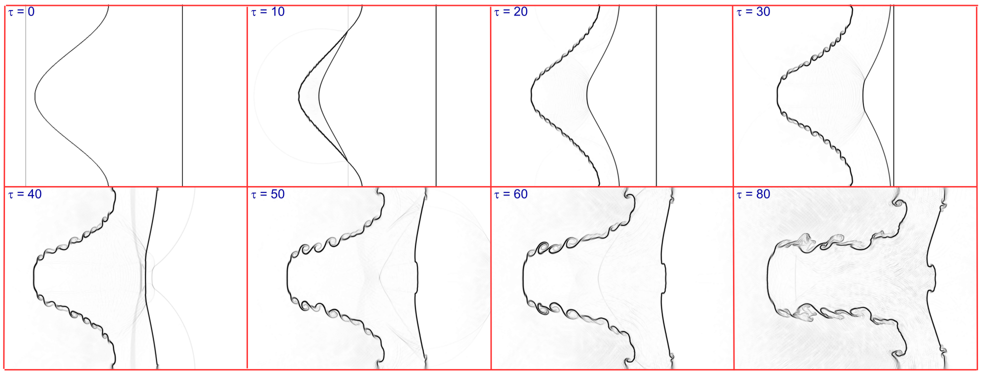

(b) d = 40

Figure 12. Temporal evolution of numerical Schlieren fields for the 2D shock-driven single-mode SF_6 fluid layer, highlighting the effect of the fluid-layer thickness: (a) $d = 5$mm and (b) $d = 40$mm, for $a_0 = 15$mm, $\lambda = 100$mm, and $M_s = 1.21$.

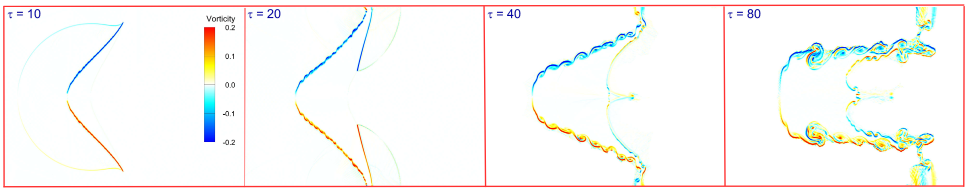

(a) d= 5

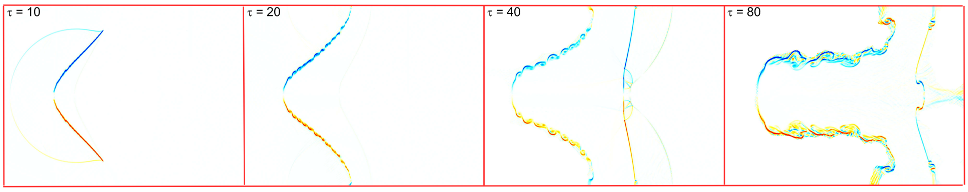

(b) d = 40

Figure 13. Temporal evolution of vorticity flow fields for the 2D shock-driven single-mode SF_6 fluid layer, highlighting the effect of the fluid-layer thickness: (a) $d = 5$mm and (b) $d = 40$mm, for $a_0 = 15$mm, $\lambda = 100$mm, and $M_s = 1.21$.

To further quantify the development of the shock-driven interface instability, we employ integral diagnostics based on the spatially integrated baroclinic vorticity and enstrophy. These global measures provide insight into the amplification of vorticity and the degree of interface deformation during the evolution of the shock-driven heavy fluid layer.

The absolute baroclinic vorticity, which reflects the local production of vorticity due to the baroclinic torque, is defined as

$$|\omega_{\mathrm{bar}}|(\tau) = \int_D \left| \frac{1}{\rho^2} (\nabla\rho \times \nabla p) \right| dx\,dy, \tag{4.10}$$

where D denotes the computational domain. The overall strength of the vorticity field is characterized by the enstrophy Ω, defined as

$$\Omega(\tau) = \int_D \omega^2\, dx\,dy, \tag{4.11}$$

with ω denoting the scalar vorticity. A rise in $|\omega_{\mathrm{bar}}|$ or Ω indicates enhanced vorticity generation and interface roll-up, whereas a reduction reflects the attenuation of the instability or the redistribution of vortical energy.

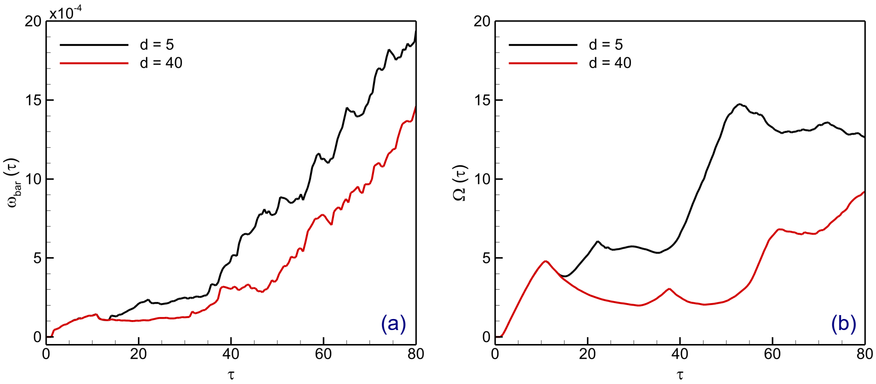

Figure 14. Influence of fluid-layer thickness ($d = 5$ and 40mm) on the 2D shock-driven single-mode SF$_6$ layer at $a_0 = 15$mm and $M_s = 1.21$: temporal evolution of spatially integrated fields of (a) baroclinic vorticity (ω_{bar}) and (b) enstrophy (Ω).

Figure 14 shows the temporal evolution of the spatially integrated baroclinic vorticity and enstrophy for two different fluid-layer thicknesses. The growth of these integral quantities reflects the progressive amplification of vorticity and the transition of the interface from linear deformation to nonlinear roll-up. In Figure 14(a), the baroclinic vorticity ω_{bar} increases immediately after shock impact and grows monotonically with time for both cases. However, the growth is noticeably faster for the thin layer ($d =$ 5mm) due to the early reinteraction of reflected waves with the interface, which enhances the baroclinic torque and strengthens vorticity production. For the thicker layer ($d = 40$mm), the transmitted shock reaches the downstream interface later, and the absence of early wave-interface interactions leads to a more gradual vorticity increase. Figure 14(b) shows the corresponding evolution of the enstrophy Ω, which represents the global strength of the vortical field. For the thin layer, Ω increases rapidly after $\tau \approx 20$, coinciding with the onset of vortex roll-up, and reaches a larger peak value at approximately $\tau \approx 60$. On the contrary, the thick layer shows a slower and smaller increase of Ω, with a lower peak level, suggesting that the creation of small-scale structures is repressed and the production of large-scale vortices is delayed. All things considered, the curves support the idea that reducing the layer thickness accelerates the transition to the nonlinear stage of shock-driven instability and increases the production of vorticity.

5. Concluding remarks

In this study, a high-order mixed LDG scheme was developed and systematically evaluated for simulating shock-driven instabilities in compressible multicomponent flows. The formulation employs a mixed first-order representation of the viscous and diffusive terms, enabling a consistent treatment of the NSF equations within the LDG framework. The scheme combines high spectral accuracy in smooth regions with robust shock-capturing capability achieved through a modal moment limiter and an alternating diffusive-flux strategy. The accuracy and stability of the method were verified through a sequence of canonical test cases. The 1D and 2D advection problems demonstrated the optimal order convergence. Subsequent validation on the Sod shock tube, cylindrical interfaces (heavy and light), and chevron-shaped configurations confirmed the solver's ability to capture key physical mechanisms, including shock refraction, baroclinic vorticity deposition, vortex roll-up, and interface deformation, with excellent agreement with experimental and reference numerical data. Furthermore, we also studied a 2D shock-driven heavy fluid layer in which a planar shock interacts with a perturbed dense-light interface, leading to baroclinic vorticity generation, vortex roll-up, and subsequent interface deformation. Parametric investigations revealed that thinner heavy-gas layers intensify baroclinic torque and promote an earlier transition to the nonlinear regime, whereas thicker layers delay vortex interactions and suppress small-scale mixing. Integral analyses of baroclinic vorticity and enstrophy further demonstrated that geometric confinement plays a crucial role in modulating vorticity generation and interface evolution. Overall, the proposed mixed LDG framework exhibits excellent robustness and accuracy for simulating complex shock-interface interactions in compressible multicomponent flows. Future developments will focus on extending the present formulation to fully three-dimensional and multi-layer configurations, where additional instability mechanisms become active. Moreover, incorporating non-equilibrium transport and reactive flow models will further enhance the predictive capability of the LDG solver for high-Mach-number shock-driven systems.

Author contributions

Satyvir Singh: Conceptualization, Software, Formal analysis, Visualization, Investigation, Validation, Writing–original draft; Salman Saud Alsaeed: Formal analysis, Investigation, Writing–review draft, Funding acquisition. All authors have read and agreed to the published version of the manuscript.

Use of Generative-AI tools declaration

The authors declare they have not used Artificial Intelligence (AI) tools in the creation of this article.

Acknowledgments

This work was funded by the Deanship of Graduate Studies and Scientific Research at Jouf University under Grant No. (DGSSR-2025-FC-01034).

Conflict of interest

The authors declare that they have no conflicts of interest.

References

1. Y. Zhou, *Hydrodynamic instabilities and turbulence: Rayleigh-Taylor, Richtmyer-Meshkov, and Kelvin-Helmholtz mixing*, Cambridge University Press, 2024.
2. Y. Zhou, Rayleigh-Taylor and Richtmyer-Meshkov instability induced flow, turbulence, and mixing. I, *Phys. Rep.*, **720–722** (2017), 1–136. https://doi.org/10.1016/j.physrep.2017.07.005
3. Y. Zhou, Rayleigh-Taylor and Richtmyer-Meshkov instability induced flow, turbulence, and mixing. II, *Phys. Rep.*, **723–725** (2017), 1–160. https://doi.org/10.1016/j.physrep.2017.07.008
4. R. Abgrall, S. Karni, Computations of compressible multifluids, *J. Comput. Phys.*, **169** (2001), 594–623. https://doi.org/10.1006/jcph.2000.6685
5. R. Saurel, O. Lemetayer, A multiphase model for compressible flows with interfaces, shocks, detonation waves and cavitation, *J. Fluid Mech.*, **431** (2001), 239–271. https://doi.org/10.1017/S0022112000003098
6. S. K. Shankar, S. Kawai, S. K. Lele, Two-dimensional viscous flow simulation of a shock accelerated heavy gas cylinder, *Phys. Fluids*, **23** (2011), 024102. https://doi.org/10.1063/1.3553282
7. J. Lindl, O. Landen, J. Edwards, E. Moses, N. Team, Review of the National Ignition Campaign 2009–2012, *Phys. Plasmas*, **21** (2014), 020501. https://doi.org/10.1063/1.4865400
8. J. Yang, T. Kubota, E. E. Zukoski, Applications of shock-induced mixing to supersonic combustion, *AIAA J.*, **31** (1993), 854–862. https://doi.org/10.2514/3.11696
9. X. D. Cai, R. Deiterding, J. H. Liang, M. B. Sun, Y. Mahmoudi, Diffusion and mixing effects in hot jet initiation and propagation of hydrogen detonations, *J. Fluid Mech.*, **836** (2018), 324–351. https://doi.org/10.1017/jfm.2017.770
10. C. C. Kuranz, H. S. Park, C. M. Huntington, A. R. Miles, B. A. Remington, T. Plewa, et al., How high energy fluxes may affect Rayleigh-Taylor instability growth in young supernova remnants, *Nat. Commun.*, **9** (2018), 1564.
11. R. D. Richtmyer, Taylor instability in shock acceleration of compressible fluids, *Commun. Pure Appl. Math.*, **13** (1960), 297–319. https://doi.org/10.1002/cpa.3160130207
12. E. E. Meshkov, Instability of the interface of two gases accelerated by a shock wave, *Fluid Dyn.*, **4** (1969), 101–104. https://doi.org/10.1007/BF01015969
13. D. Ranjan, J. Oakley, R. Bonazza, Shock-bubble interactions, *Annu. Rev. Fluid Mech.*, **43** (2011), 117–140. https://doi.org/10.1146/annurev-fluid-122109-160744

14. M. Brouillette, The Richtmyer-Meshkov instability, *Annu. Rev. Fluid Mech.*, **34** (2002), 445–468. https://doi.org/10.1146/annurev.fluid.34.090101.162238

15. K. Ferguson, J. W. Jacobs, The influence of the shock-to-reshock time on the Richtmyer-Meshkov instability in reshock, *J. Fluid Mech.*, **999** (2024), A68. https://doi.org/10.1017/jfm.2024.795

16. R. Saurel, C. Pantano, Diffuse-interface capturing methods for compressible two-phase flows, *Annu. Rev. Fluid Mech.*, **50** (2018), 105–130. https://doi.org/10.1146/annurev-fluid-122316-050109

17. V. Maltsev, M. Skote, P. Tsoutsanis, High-order methods for diffuse-interface models in compressible multi-medium flows: a review, *Phys. Fluids*, **34** (2022), 021301. https://doi.org/10.1063/5.0077314

18. M. Latini, O. Schilling, W. S. Don, Effects of WENO flux reconstruction order and spatial resolution on reshocked two-dimensional Richtmyer-Meshkov instability, *J. Comput. Phys.*, **221** (2007), 805–836. https://doi.org/10.1016/j.jcp.2006.06.051

19. X. Lei, J. Q. Li, A non-oscillatory energy-splitting method for the computation of compressible multi-fluid flows, *Phys. Fluids*, **30** (2018), 040906. https://doi.org/10.1063/1.5011093

20. S. C. Pan, L. H. Han, X. Y. Hu, N. A. Adams, A conservative interface-interaction method for compressible multi-material flows, *J. Comput. Phys.*, **371** (2018), 870–895. https://doi.org/10.1016/j.jcp.2018.02.007

21. J. Luo, X. Y. Hu, N. A. Adams, Efficient formulation of scale separation for multi-scale modeling of interfacial flows, *J. Comput. Phys.*, **308** (2016), 411–420. https://doi.org/10.1016/j.jcp.2015.11.044

22. B. Thornber, M. Groom, D. Youngs, A five-equation model for the simulation of miscible and viscous compressible fluids, *J. Comput. Phys.*, **372** (2018), 256–280. https://doi.org/10.1016/j.jcp.2018.06.028

23. M. Hahn, D. Drikakis, D. L. Youngs, R. J. R. Williams, Richtmyer-Meshkov turbulent mixing arising from an inclined material interface with realistic surface perturbations and reshocked flow, *Phys. Fluids*, **23** (2011), 046101. https://doi.org/10.1063/1.3576187

24. H. C. Yee, B. Sjögreen, Numerical dissipation control in high-order methods for compressible turbulence: recent development, *Fluids*, **9** (2024), 1–70. https://doi.org/10.3390/fluids9060127

25. Q. J. Wang, R. Deiterding, J. H. Pan, Y. X. Ren, Consistent high resolution interface-capturing finite volume method for compressible multi-material flows, *Comput. Fluids*, **202** (2020), 104518. https://doi.org/10.1016/j.compfluid.2020.104518

26. P. Tsoutsanis, E. M. Adebayo, A. C. Merino, A. P. Arjona, M. Skote, CWENO finite-volume interface capturing schemes for multicomponent flows using unstructured meshes, *J. Sci. Comput.*, **89** (2021), 64. https://doi.org/10.1007/s10915-021-01673-y

27. J. Giordano, Y. Burtschel, Richtmyer-Meshkov instability induced by shock-bubble interaction: numerical and analytical studies with experimental validation, *Phys. Fluids*, **18** (2006), 036102. https://doi.org/10.1063/1.2185685

28. S. Chapman, T. G. Cowling, *The mathematical theory of non-uniform gases: an account of the kinetic theory of viscosity, thermal conduction and diffusion in gases*, Cambridge University Press, 1990.
29. C. R. Wilke, A viscosity equation for gas mixtures, *J. Chem. Phys.*, **18** (1950), 517–519. https://doi.org/10.1063/1.1747673
30. B. Cockburn, C. W. Shu, The local discontinuous Galerkin method for time-dependent convection-diffusion systems, *SIAM J. Numer. Anal.*, **35** (1998), 2440–2463. https://doi.org/10.1137/S0036142997316712
31. S. Singh, A. Karchani, T. Chourushi, R. S. Myong, A three-dimensional modal discontinuous Galerkin method for the second-order Boltzmann-Curtiss-based constitutive model of rarefied and microscale gas flows, *J. Comput. Phys.*, **457** (2022), 111052. https://doi.org/10.1016/j.jcp.2022.111052
32. S. Singh, *Development of a 3D discontinuous Galerkin method for the second-order Boltzmann-Curtiss based hydrodynamic models of diatomic and polyatomic gases*, Ph.D. thesis, Gyeongsang National University, 2018.
33. E. Johnsen, T. Colonius, Implementation of WENO schemes in compressible multicomponent flow problems, *J. Comput. Phys.*, **219** (2006), 715–732. https://doi.org/10.1016/j.jcp.2006.04.018
34. L. Krivodonova, Limiters for high-order discontinuous Galerkin methods, *J. Comput. Phys.*, **226** (2007), 879–896. https://doi.org/10.1016/j.jcp.2007.05.011
35. D. I. Ketcheson, Highly efficient strong stability-preserving Runge-Kutta methods with low-storage implementations, *SIAM J. Sci. Comput.*, **30** (2008), 2113–2136. https://doi.org/10.1137/07070485X
36. J. F. Haas, B. Sturtevant, Interaction of weak shock waves with cylindrical and spherical gas inhomogeneities, *J. Fluid Mech.*, **181** (1987), 41–76. https://doi.org/10.1017/S0022112087002003
37. J. J. Quirk, S. Karni, On the dynamics of a shock-bubble interaction, *J. Fluid Mech.*, **318** (1996), 129–163. https://doi.org/10.1017/S0022112096007069
38. X. S. Luo, P. Dong, T. Si, Z. G. Zhai, The Richtmyer-Meshkov instability of a 'V'shaped air/SF_6 interface, *J. Fluid Mech.*, **802** (2016), 186–202. https://doi.org/10.1017/jfm.2016.476
39. S. S. Alsaeed, S. Satyvir, N. A. Alrubea, Numerical investigation of Atwood number effects on shock-driven single-mode stratified heavy fluid layer, *Mathematics*, **13** (2025), 1–26. https://doi.org/10.3390/math13183032
40. S. S. Alsaeed, S. Satyvir, N. A. Alrubea, Layer thickness impact on shock-accelerated interfacial instabilities in single-mode stratifications, *Appl. Sci.*, **15** (2025), 1–26. https://doi.org/10.3390/app151910687